

PAPER

Peak-Persistence Diagrams for Estimating Shapes and Functions from Noisy Data

Woo Min Kim,¹ Sutanoy Dasgupta² and Anuj Srivastava^{1,*}¹Dept of Statistics, Florida State University, Tallahassee, 32306, FL, USA and ²Dept of Statistics, Texas A&M University, College Station, 77843, TX, USA

*Corresponding author. anuj@stat.fsu.edu

FOR PUBLISHER ONLY Received on Date Month Year; revised on Date Month Year; accepted on Date Month Year

Abstract

Estimating signals underlying noisy data is a significant problem in statistics and engineering. Numerous estimators are available in the literature, depending on the observation model and estimation criterion. This paper introduces a framework that estimates the shape of the unknown signal and the signal itself. The approach utilizes a peak-persistence diagram (PPD), a novel tool that explores the dominant peaks in the potential solutions and estimates the function's shape, which includes the number of internal peaks and valleys. It then imposes this shape constraint on the search space and estimates the signal from partially-aligned data. This approach balances two previous solutions: averaging without alignment and averaging with complete elastic alignment. From a statistical viewpoint, it achieves an optimal estimator under a model with both additive noise and phase or warping noise. We also present a computationally-efficient procedure for implementing this solution and demonstrate its effectiveness on several simulated and real examples. Notably, this geometric approach outperforms the current state-of-the-art in the field.

Key words: functional data analysis, function estimation, peak persistence diagram, SRVF, peak-constrained curve estimation, shape estimation.

Introduction

Analyzing noisy data to estimate underlying signals or some relevant properties is a fundamental problem in statistics and engineering. One models the observed data as an actual underlying signal corrupted by noise, and the goal is to use data to estimate that signal. The choice of an estimator depends on the observation model, the noise distribution, the data structure, and the optimization criterion. The classical approach to

function estimation is to identify a function space (typically a Hilbert space with an orthonormal basis), impose an objective function, and optimize it over the function space. Our approach is slightly different. We will focus on the shapes of functions and introduce a novel tool, the peak-persistence diagram (PPD), to search for the estimate. This PPD enables us to estimate the shape of an unknown function first, followed by a shape-constrained estimation of the function itself.

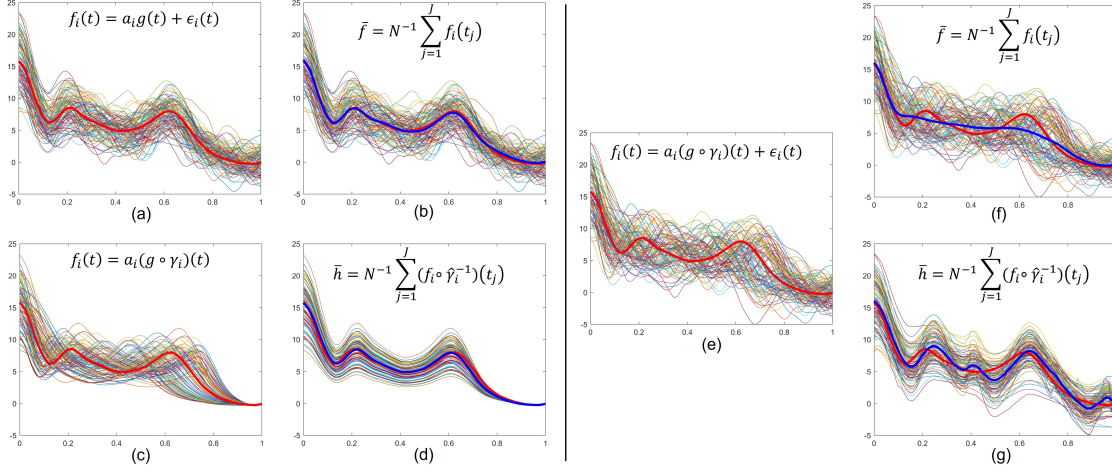


Fig. 1. Bold red lines denote g , blue lines in (b),(f) denote \bar{f} , and blue lines in (d),(g) denote \bar{h} . Functions in (a) have additive noise only, and those in (c) have phase noise only. Functions in (e) contain both additive and phase noises. The estimations in (b) and (d) perform well, whereas those in (f) and (g) do not.

We start from a traditional perspective on the function estimation problem and later make a case for a geometric (shape-based) approach. A simple, traditional model for function estimation is the **additive noise model**:

$$f_i(t) = a_i g(t) + \epsilon_i(t), \quad i = 1, 2, \dots, n, \quad (1)$$

where $g \in \mathcal{F}$ is the unknown signal, $\epsilon_i \in \mathcal{F}$ is the zero mean, independent noise and $a_i \in \mathbb{R}$ is an independent random variable with mean one. Here \mathcal{F} denotes a functional space of interest; most commonly, \mathcal{F} is the Hilbert space of square-integrable functions on an interval. In a simple case, with dense time samples, an estimate of g is given by the *cross-sectional mean* $\bar{f} = \frac{1}{n} \sum_{i=1}^n f_i$, because $\frac{1}{n} \sum_{i=1}^n \epsilon_i \rightarrow 0$ and $\frac{1}{n} \sum_{i=1}^n a_i \rightarrow 1$. The top left part of Fig. 1 shows a pictorial illustration of this estimation. Plot (a) shows the data $\{f_i\}$ and the true function g (in red), and (b) shows their cross-sectional mean superimposed in blue. In case of sparse data or other challenges, one can utilize a smooth basis for g or add a roughness penalty (or a prior) to the standard least-squares objective function (Ramsay and Silverman (1997); Fan and Gijbels (1996); Choudhuri et al. (2005); Green and Silverman (1994)).

In recent years, there has been a growing recognition of a different kind of noise or variability in functional data, the so-called *phase* or *compositional* noise. The observation model for this noise is given by the **phase noise model**:

$$f_i(t) = g(\gamma_i(t)), \quad i = 1, 2, \dots, n, \quad (2)$$

where γ_i s are random time-warping functions of the domain. (A precise mathematical definition of time-warping functions is presented later.) To have identifiable g , one assumes that the phase noise has identity mean, *i. e.*, $\frac{1}{n} \sum_{i=1}^n \gamma_i(t) \rightarrow t$. One can verify that, in this case, the cross-sectional mean \bar{f} does not directly estimate g . This is because $\frac{1}{n} \sum_{i=1}^n g(\gamma_i(t))$ does not converge to $g(t)$, in general, despite the fact that $(\frac{1}{n} \sum_{i=1}^n \gamma_i(t)) \mapsto t$. The quantity $\lim_{n \rightarrow \infty} \frac{1}{n} \sum_{i=1}^n g(\gamma_i(t))$ can be approximated by $\int g(t+x)\pi(x) dx$, where π is a normal density, and thus, the result is a Gaussian blurring of g . The estimation solution comes from solving for the γ_i s explicitly and then performing an alignment of given data according to $\{\tilde{f}_i = f_i \circ \hat{\gamma}_i^{-1}\}$. This alignment is also called *phase-amplitude separation* in the literature (Ramsay and Li (1998); Srivastava and Klassen (2016); Srivastava et al. (2011); Marron et al. (2015)). One can then estimate g using cross-sectional averaging of the *aligned functions* $\frac{1}{n} \sum_{i=1}^n \tilde{f}_i$ (Kurtek et al. (2011)). We will call this average quantity the *fully-elastic mean*. The bottom left part of Fig. 1 shows a pictorial illustration of this estimation. Plot (c) shows the data $\{f_i\}$ and the true function g (in red), and (d) shows the aligned functions $\{\tilde{f}_i\}$ and their mean superimposed in blue. While there are several approaches in the literature for functional alignment (see, e.g., Kneip and Ramsay (2008); Liu and Muller (2004); Marron et al. (2015)), a particularly efficient method is based on the nonparametric Fisher-Rao metric (Srivastava and Klassen (2016); Srivastava et al. (2011)). It uses a square-root representation of functions and a dynamic

programming (DP) algorithm to estimate $\{\hat{\gamma}_i\}$ and is remarkably successful in aligning peaks and valleys of f_i s. The example shown in (d) uses this method.

Problem Specification

This paper focuses on a more general problem where *both* additive and phase noise are present in the data. The observation model is now given by the **additive and phase noise model**:

$$f_i(t) = a_i(g \circ \gamma_i)(t) + \epsilon_i(t), \quad i = 1, 2, \dots, n. \quad (3)$$

The components of the model remain the same as earlier. Next, we discuss the current state-of-the-art in handling this model.

Past Methods

There has been some research on function estimation under the model specified in Eqn. 3. A seemingly natural idea for estimating g is the least square solution:

$$\operatorname{argmin}_{g \in \mathcal{F}} \left(\sum_{i=1}^n \min_{a_i \in \mathbb{R}, \gamma_i \in \Gamma} \left(\|f_i - a_i(g \circ \gamma_i)\|^2 + \kappa \mathcal{R}(\gamma_i) \right) \right), \quad (4)$$

where \mathcal{R} denotes a roughness penalty on γ_i s. However, this optimization has several problems. Firstly, for $\kappa = 0$, the optimization over γ_i s is degenerate; this phenomenon is called the *pinching effect* (Ramsay and Silverman (1997); Srivastava and Klassen (2016)). While adding a penalty term (setting $\kappa > 0$) may avoid degeneracy, it does not entirely solve the problem. It limits the search space for a solution and can have unintended consequences. Also, determining the optimal value for the penalty parameter κ in Eqn. 4 is known to be a challenging task. Different values of κ may lead to widely different solutions (examples are provided later in Section 2).

Some past papers (Kneip and Ramsay (2008); Ramsay and Li (1998); Tang and Muller (2008); Earls and Hooker (2017)) have used Eqn. 4 but with a focus on aligning functional data. Marron et al. (2015) provide a survey of papers on functional alignment. Some others have studied a mixed-effects model by adding a random effect term to Eqn. 3 (Raket et al. (2014); Claeskens et al. (2021)). A similar problem has been investigated in the registration of images (Allasonnière et al. (2007); Simpson et al. (2012)), albeit with focus on preserving visual features. Almost all these papers use the \mathbb{L}^2 objective function and must balance the two terms in Eqn.4. Also, some papers have pursued a Bayesian approach for the alignment of given data $\{f_i\}$ by imposing a prior on γ_i s (Kurtek (2017)). Some papers advocate smoothing the given functions and then computing averages (Cheng et al. (2013); Lu et al. (2017); Telesca

and Inoue (2008)). However, these papers do not explicitly estimate the signal g . One can also impose a prior on g to formulate a Bayesian solution, as in Matuk et al. (2021); Horton et al. (2020). This approach requires specific prior information about g to be effective.

We are going to pursue a geometric approach and discuss related literature. Some papers have studied the estimation of the so-called Procrustes means of "shapes" of Euclidean curves (Stöcker et al., 2022), but they do not provide an estimator of g . There also exists literature on shape-constrained density estimation but often restricted to a narrow shape class. This large body of work started with Grenander (1956) and followed by several (Wang and Berger (2016); Cheng et al. (1999); Wegman (1970); Doss and Wellner (2016)). This effort is restricted to unimodal or log-concave shape classes rather than general shapes. Please refer to the special issue (Samworth and Sen (2018)) for a recent overview of that field. We note that Dasgupta et al. (2021) generalized the problem to general shape classes but still restricted the estimation to densities. The current paper looks at general functions under arbitrary shape constraints.

Lastly, we mention sparse literature on estimating the number of modes of probability density underlying given data. There are some papers (see e.g. Minnotte (1997)) that study estimation of multiple modes in density functions but most of the past literature is focused on the narrow case of unimodal functions. Our problem differs from density estimation in that we are dealing with functional data.

Our Approach

Our approach adopts a geometric perspective that focuses on function shapes. It is motivated by the fact that Eqns. 1, 2 are special cases of Eqn. 3. We aim to strike a balance between the non-elastic and fully elastic, as neither of these solutions is satisfactory. The cross-sectional mean over-smooths the data, while the fully-elastic mean aligns even the noise artifacts, resulting in spurious peaks and valleys in the estimate. The right part of Fig. 1 shows an example: For the data in (e), plot (f) shows the non-elastic mean, and plot (g) shows the elastic mean. We argue that a good solution lies between these two extremes and is adaptive. To achieve this, we propose using partial alignments that control the elasticity of the functions during alignment via a parameter $\lambda \in \mathbb{R}_+$. The resulting partially-aligned functions are denoted $\tilde{f}_{\lambda,i}$, and their mean is denoted $\hat{g}_\lambda = \sum_{i=1}^n \tilde{f}_{\lambda,i}$. An important consideration is choosing λ adaptive to the given data. Additionally, we must address the degeneracy from the pinching effect. To tackle these issues, we apply

shape analysis techniques. Our approach varies the elasticity parameter to estimate the shape of g and g as follows:

1. **Peak-Persistence Diagram (PPD):** The objective of this stage is to estimate the shape of g by identifying its geometric features which remain invariant to phase noise. A novel tool called a Peak Persistence Diagram (PPD) has been developed for this purpose. When we change the parameter λ , the shape of the average function \hat{g}_λ changes. Typically, the geometric features, such as peaks and valleys, are smoothed out as λ increases. Therefore, a good choice of λ can be identified by studying the persistence of the internal peaks of \hat{g}_λ versus λ and selecting the most persistent peaks. A graphic display of this persistence is called a Peak Persistence Diagram or PPD. A set of heuristics is used to define criteria for selecting the most persistent peaks in a PPD. This process yields three quantities: an optimal λ^* , the number m of persistent internal peaks, and $\hat{f}_{\lambda^*,i}$, which is the partially aligned data for the optimal weight λ^* .
2. **Shape-Constrained Function Estimation:** The preceding step generates a partially-aligned mean \hat{g}_{λ^*} . This is an element of the correct shape class, but may not be the optimal estimate of g in a precise sense. Therefore, in the second step, we aim to find the optimal element in the chosen class. We constrain the estimate of g to have precisely m internal peaks and utilize a geometric approach to perform a shape-constrained estimation of g . The estimation process involves minimizing the squared error over the appropriate constraint space \mathcal{F}_m , using the data $\hat{f}_{\lambda^*,i}$. Here, \mathcal{F}_m refers to the set of all elements of \mathcal{F} that have the correct shape, *i. e.*, m internal peaks. This approach differs from previous shape-constrained estimators since it provides a penalized-MLE in \mathcal{F}_m , rather than an arbitrary element of \mathcal{F}_m .

In this paper we have focused on only the *internal* peaks and valleys of g . The potential peaks at the boundaries are also relevant but they can be detected separately using simple tests and are ignored here.

Penalized \mathbb{L}^2 Estimator

Before we lay out the proposed framework, we further elaborate on the issues facing a solution based on Eqn. 4. There are two main issues: (1) The problem is degenerate for $\kappa = 0$, giving rise to the *pinching effect*, and (2) How should one set the value of κ to avoid over smoothing and pinching? Although there

are several ideas in the literature on choosing the smoothing parameter, pinching makes this selection complicated. One typically needs higher values of κ to avoid pinching but that can result in oversmoothing. We illustrate this with an example using the first order roughness penalty $R(\gamma_i) = \int (1 - \sqrt{\gamma_i(t)})^2 dt$. (The detailed algorithm is presented in Srivastava and Klassen (2016).) Fig. 2 (a) displays the given functions $\{f_i\}$ and their cross-sectional mean \bar{f} (depicted in blue). The red curves represent the ground truth, g , and the blue curves in plots (b)-(e) denote the cross-section mean of aligned curves, denoted by \hat{g}_{L^2} . At $\kappa = 0 \sim 1$, one can see the pinching effects in the estimate, but as κ increases, the estimate gets smoother. This example shows that a carefully chosen κ is needed to reach a good estimate of g . The challenge is finding an automated technique for optimal κ while avoiding pinching.

Our shape-based framework differs from Eqn. 4 in that the formulation is developed using the Fisher-Rao distance rather than the \mathbb{L}^2 distance, and it avoids the pinching problem altogether. However, the issue of choosing the smoothing parameter remains, and we tackle it using PPDs. For the remainder of this paper, we will assume that the functional data is defined on a compact interval I and \mathcal{F} is the set of all absolutely-continuous, real-valued functions on I . We will consider the model stated in Eqn. 3, with following independent components: (1) Scaling noise: $a_i \in \mathbb{R}^+ \sim N(1, \sigma_a^2)$; (2) Additive noise: $\epsilon_i \in \mathcal{F}$, a random function with mean $E[\epsilon_i(t)] = 0$ for all $t \in I$; (3) Phase noise: $\gamma_i \in \Gamma$ (where Γ is defined below), with the mean $E[\gamma_i(t)] = \gamma_{id}(t) = t$. Given a set of independent observations $\{f_i\}$, our goal is to estimate the number of internal peaks in g and the function g itself.

Step 1: Shape Estimation Using PPDs

The goal here is to estimate the shape of g , *i. e.*, estimate the number of internal peaks and valleys in g , from the given $\{f_i\}$ and form an initial estimate of g .

Background Material: We summarize a mechanism for partial elastic alignments of functions under the Fisher-Rao metric and refer the reader to Srivastava and Klassen (2016) for details. For alignment purposes, a function $f \in \mathcal{F}$ is represented by its square-root velocity function (SRVF): $q(t) = \text{sign}(\dot{f}(t))\sqrt{|\dot{f}(t)|}$. Let Γ denote the group of all boundary-preserving diffeomorphisms of I . Any element $\gamma \in \Gamma$ is a smooth function with a smooth inverse and preserves the boundaries of I . The set Γ forms a group under composition, *i. e.*, for any $\gamma_1, \gamma_2 \in \Gamma$, we have $\gamma_1 \circ \gamma_2 \in \Gamma$. This group has an

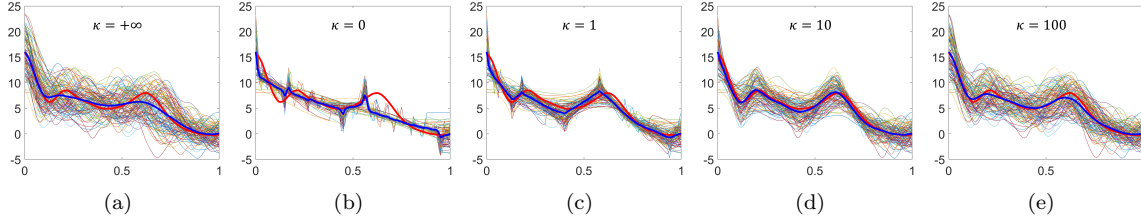


Fig. 2. Alignments of given functions and estimates of g according to Eqn. 4. Plot (a) show the original functions and their mean (blue). Plots (b)-(e) show the true g (red), the partially-aligned set, and the estimates (blue curves) for different κ .

identity element $\gamma_{id}(t) = t$. Let a function $f \in \mathcal{F}$ be time-warped by any $\gamma \in \Gamma$, resulting in $f \circ \gamma$. The SRVF of the warped function is given by $(q \circ \gamma)\sqrt{\dot{\gamma}}$, and we will denote it by $q \star \gamma$ for brevity.

With this setup, we can solve for elastic alignment of any two functions $f_1, f_2 \in \mathcal{F}$ as follows. Let q_1, q_2 denote the SRVFs of f_1, f_2 , respectively. Then, the optimal time warping to align f_2 to f_1 is given by: $\gamma^* = \operatorname{argmin}_{\gamma \in \Gamma} \|q_1 - (q_2 \star \gamma)\|^2$, where $\|\cdot\|$ denotes the \mathbb{L}^2 norm. However, if we want to penalize the level of elasticity in their alignment, we can do so using: $\operatorname{argmin}_{\gamma \in \Gamma} (\|q_1 - (q_2 \star \gamma)\|^2 + \lambda \mathcal{R}(\gamma))$. The term $\mathcal{R}(\gamma)$ denotes a penalty on the roughness of γ and forces it to be close to the identity element γ_{id} . (In this paper, we have chosen the first-order penalty $\mathcal{R} = \|1 - \sqrt{\dot{\gamma}}\|^2$, but one can use other penalties instead.) The constant $\lambda > 0$ controls the amount of elasticity in the alignment: $\lambda = 0$ is fully elastic and $\lambda = \infty$ is non elastic. To align multiple functions, say f_1, f_2, \dots, f_n , let q_1, q_2, \dots, q_n denotes their respective SRVFs. Then, a joint alignment of these functions is performed using the following optimization:

$$\min_{q \in \mathbb{L}^2} \left[\sum_{i=1}^n \left(\min_{\gamma_i \in \Gamma} (\|q - (q_i \star \gamma_i)\|^2 + \lambda \mathcal{R}(\gamma_i)) \right) \right]. \quad (5)$$

We can rearrange this equation using the facts that $\|q_1 - q_2 \star \gamma\| = \|q_1 \star \gamma^{-1} - q_2\|$, for all $q_1, q_2 \in \mathbb{L}^2$ and $\gamma \in \Gamma$, and that Γ is a group. This results in:

$$\min_{q \in \mathbb{L}^2} \left[\sum_{i=1}^n \left(\min_{\gamma_i \in \Gamma} (\|q_i - (q \star \gamma_i)\|^2 + \lambda \mathcal{R}(\gamma_i)) \right) \right],$$

which can be directly compared to Eqn. 4. (Note that we ignore the optimization over a_i s here as they average out in any mean-based estimation.) The main difference between the two solutions lies in the use of SRVFs and the invariance properties of the elastic metric. Fundamentally, the difference comes from the fact that $\|q\| = \|q \star \gamma\|$, for all $q \in \mathbb{L}^2$ and $\gamma \in \Gamma$, while $\|f\| \neq \|f \circ \gamma\|$ in general.

The SRVF-based optimization (Eqn. 5) does not provide an estimate of g directly but results in

several quantities of interest: (1) If $\hat{\gamma}_{\lambda, i}$ denotes the optimal time warping inside the summation, for each i , then $\tilde{f}_{\lambda, i} = f_i \circ \hat{\gamma}_{\lambda, i}$ are the resulting partially-aligned functions; (2) Let \hat{g}_λ be the cross-sectional mean of these $\tilde{f}_{\lambda, i}$. Algorithm 1 summarizes the main steps in this partial elastic alignment. Fig. 3

Algorithm 1 Function-Alignment Algorithm

Require: Data $\{f_1, f_2, \dots, f_n\}$

```

1: for  $i = 1, \dots, n$  do
2:    $q_i \leftarrow \operatorname{sign}(\dot{f}_i) \sqrt{|\dot{f}_i|}$ 
3: end for
4:  $\bar{q} \leftarrow \operatorname{argmin}_{q \in \{q_1, \dots, q_n\}} \|q - \frac{1}{n} \sum_{i=1}^n q_i\|$ 
5: while  $\epsilon > \operatorname{tol}$  do
6:   for  $i = 1, 2, \dots, n$  do
7:      $\hat{\gamma}_{\lambda, i} \leftarrow \operatorname{arg inf}_{\gamma \in \Gamma} (\|\bar{q} - (q_i \star \gamma)\|^2 + \lambda \mathcal{R})$ 
8:      $f_i^* \leftarrow f_i \circ \hat{\gamma}_{\lambda, i}$ , and  $q_i^* \leftarrow \operatorname{sign}(\dot{f}_i^*) \sqrt{|\dot{f}_i^*|}$ 
9:   end for
10:   $\bar{q}^* \leftarrow \frac{1}{n} \sum_{i=1}^n q_i^*$ ,  $\epsilon \leftarrow \|\bar{q} - \bar{q}^*\|^2$ 
11:  if  $\epsilon > \operatorname{tol}$  then
12:     $\bar{q} \leftarrow \bar{q}^*$ 
13:  end if
14: end while
15:  $\bar{\gamma}^{-1} \leftarrow (\frac{1}{n} \sum_{i=1}^n \hat{\gamma}_{\lambda, i})^{-1}$ ,  $\bar{q}^* \leftarrow (\bar{q}^* \star \bar{\gamma}^{-1})$ 
16: for  $i = 1, 2, \dots, n$  do
17:   $\hat{\gamma}_{\lambda, i} \leftarrow \operatorname{arg inf}_{\gamma_i \in \Gamma} (\|\bar{q}^* - (q_i \star \gamma_i)\|^2 + \lambda \mathcal{R})$ 
18:   $\tilde{f}_{\lambda, i} \leftarrow f_i \circ \hat{\gamma}_{\lambda, i}$ 
19: end for
20: return  $\hat{g}_\lambda = \frac{1}{n} \sum_{i=1}^n \tilde{f}_{\lambda, i}$ 

```

shows an illustration of the output of Algorithm 1. It offers several results, each showing partially-aligned functions and their cross-sectional mean for a different value of λ . The original data is shown in the bottom right panel. On one extreme, $\lambda = 0$ results in a perfect alignment of peaks and valleys. Conversely, $\lambda = \infty$ provides no alignment at all.

Given this context, the subsequent task involves discovering an automated method to select the best λ from the available data. This is achieved by utilizing

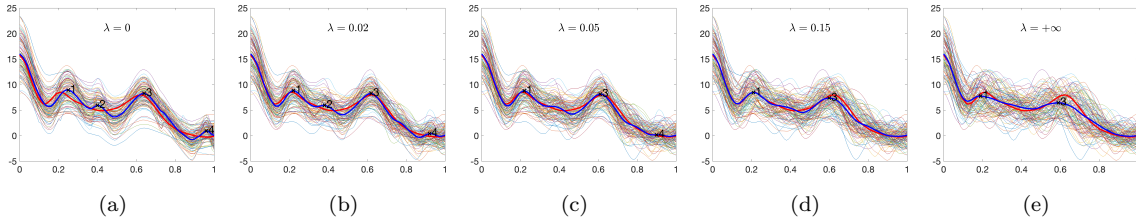


Fig. 3. Partial elastic alignments for different values of λ according to Eqn. 5. Each plot shows the true g (red), the partially aligned set $\{\hat{f}_{\lambda,i}\}$, and their cross-sectional mean \hat{g}_λ (blue curve).

the peak persistence diagram, which is introduced next.

Peak Persistence Diagrams

As λ changes from 0 to ∞ , some peaks and valleys in \hat{g}_λ start to diminish and even disappear altogether. Sometimes new peaks can also be generated. We formalize this behavior using a peak persistence diagram.

Definition 1 The peak persistence diagram (PPD) of a set of functions $\{f_i, i = 1, 2, \dots, n\}$ is a visual presentation of the **significant, internal peaks** of their partial elastic mean \hat{g}_λ plotted versus λ . Essentially, a PPD serves to identify the existence, magnitudes, and positions of significant internal peaks of \hat{g}_λ .

A PPD results in several displays. Plotting only the peak indicators across the range of λ , we obtain a PPD bar chart. If we are interested in peak locations as well, we can use a PPD surface. An important issue to address is what qualifies as a *significant* peak, which we discuss in the following subsection. The idea of tracking significant peaks has been previously utilized in density estimation (Chaudhuri and Marron (1999)), although in the context of bandwidth selection for kernel-based methods. A PPD is akin to persistence homology in topological data analysis (Zomorodian and Carlsson (2005)), where one traces the presence of topological features at different data resolutions. In contrast, a PPD tracks geometric features (peaks) for scalar functions.

Figure 4 serves as an illustration of a PPD for the data shown in 4(a). In panel (b), the PPD bar chart displays the presence of detected peaks for different values of λ . The x axis represents λ , while the y axis indicates peak labels. Panels (c) and (d) show a 3D surface plot, where the values of $\hat{g}_\lambda(t)$ are represented by colors ranging from blue to yellow, based on their height. The y axis represents λ , the x axis is t , and the labeled black lines indicate the positions of the peaks

as λ varies. At $\lambda = 0$, \hat{g}_λ exhibits four internal peaks, which change as λ increases. Notably, peaks labeled 2 and 4 disappear when $\lambda \sim 0.05$, while those labeled 1 and 3 persist.

A PPD is a useful tool for studying geometrical or shape features of the unknown function across a range of λ . Peaks that persist over a longer range are deemed significant, while those that are small or do not persist for long are attributed to noise or alignment artifacts. However, determining what is significant and what is not can be a challenging issue. In the next section, we will discuss this and other related issues.

Peak Significance and Persistence

Choosing whether a peak in a PPD is actual or an artifact is a complicated process, and one has to make some *ad hoc* choices depending on the final goal. In this paper, we focus on larger, more global structures and accept the loss of some smaller, finer features.

Significance of a peak: When is a peak considered significant? Small peaks occur in \hat{g}_λ , either due to noise or computational errors, that are not in the original g . This can happen, for example, in parts of the domain where g is constant and an alignment of noise results in spurious peaks. For a peak at t_0 , we define the *strength* of this peak to be $\frac{-\hat{g}_\lambda''(t_0)}{\|\hat{g}_\lambda'\|}$. This quantity measures the curvature at point t_0 , normalized appropriately. If this quantity is less than a predetermined value, say τ , then the peak at t_0 is considered *insignificant* and is discarded. Otherwise, it is significant and kept in PPD. This paper uses a conservative value of $\tau = 0.03$, determined through extensive experimentation and has worked well across datasets.

Persistence of a peak:

For the peak labeled k , we define its *persistence* to be $p_k = |\{\lambda \geq 0 \mid \text{peak } k \text{ in } \hat{g}_\lambda \text{ is significant}\}|$, where $|\cdot|$ denotes the length of the interval. The next issue is deciding the minimum value for a peak for it to be *persistent*. For this, we select the most persistent peak, say k_0 , and define persistence of other peaks

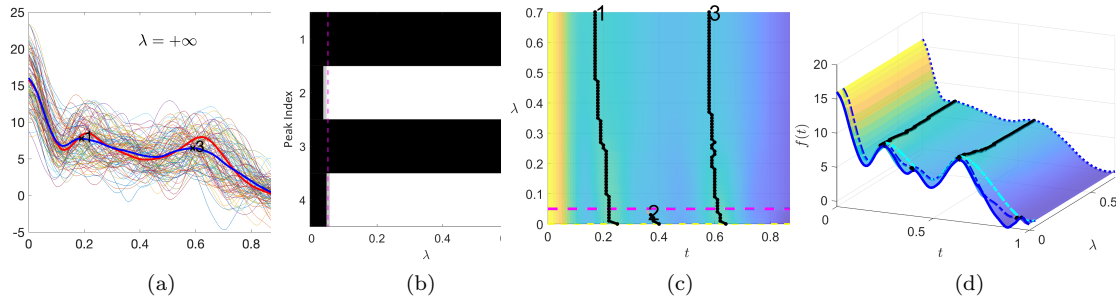


Fig. 4. (a) The original functional data, (b) the PPD bar chart, and (c), (d) PPD surface generated by interpolating \hat{g}_λ 's for different λ and the movements of the peaks.

relative to p_{k_0} . If the relative persistence of k^{th} peak p_k/p_{k_0} is larger than a threshold, say θ , then that peak is considered *persistent*. We used experiments to find that $\theta \approx 0.28$ performs best on simulated and real data. The number of internal significant peaks is then given by: $m = |\{k \geq 0 \mid p_k/p_{k_0} > \theta\}|$. This number m determines the estimated shape of g and forms a constraint in estimating g .

In summary, two hyper-parameters τ and θ are needed to determine significant and persistent peaks. The results are found to be relatively stable with respect to the choices we have made in this paper.

Selection of λ and Initial Estimate of g

Once we have selected significant and persistent internal peaks, the next step is determining an optimal value of λ , say λ^* , to help in subsequent process. We select the smallest value of λ that results in m significant peaks in \hat{g}_λ . This choice is motivated by the observations that extrema of \hat{g}_λ typically diminish as λ increases. For the example shown in Fig. 4, we select $m = 2$ and $\lambda^* = 0.05$. For this λ^* , we also compute the cross-sectional mean $\hat{g}_{\lambda^*} = \frac{1}{n} \sum_{i=1}^n \tilde{f}_{i, \lambda^*}$.

Shape Estimator Properties

It would be useful to investigate statistical properties of the estimator m of the number of internal peaks or modes in g . Several papers in the past have studied the problem of mode estimation in the context of density estimation, especially when using nonparametric kernel estimators, see *e.g.*, Minnotte (1997); Chaudhuri and Marron (1999) and references therein. Our estimator is based on the geometric properties of the cross-sectional mean \hat{g}_{λ^*} of partially-aligned functions. Given the non-Euclidean nature of the Riemannian elastic metric, and the geometric abstraction of peak persistence, we have not pursued any theoretical investigations of this

estimator. Instead, we provide extensive experimental validation of this approach using both simulated and real datasets.

Experimental Results: Shape Estimation

Now we present examples of PPD-based shape estimation on some simulated and real functional datasets.

Example 1: The first simulation generates data from a bimodal function, labeled as g_1 (red curve), which we corrupt by adding a few tri-modal curves g_2 (magenta curve). The complete set consists of 80 random perturbations of g_1 and 20 of g_2 . The objective is to investigate the estimation of the shape of g_1 from this noisy and corrupted data.

Figure 5 presents the estimation results. Plot (a) shows the original data, and (b) shows the full elastic alignment with the mean, \hat{g}_0 , drawn in blue. This mean curve has three peaks, with the third relatively small. Plot (c) shows the outcomes of partial-elastic alignment with $\lambda^* = 0.02$ chosen via PPDs displayed in panels (d), (e), and (f). The bar chart in (d) indicates two significant and persistent peaks (1 and 2), consistent with g_1 . This example suggests that the PPD method can successfully estimate the shape of the underlying signal even when the data is contaminated with another shape.

Example 2: In this instance, we have reversed the roles of g_1 and g_2 in comparison to the first simulation. Specifically, we have 80 samples of the trimodal functions and 20 samples of the bimodal functions. The fourth plot (d) in Fig. 6 demonstrates that three peaks (1, 2, and 3) are significant and persistent, and $\lambda^* = 0.01$ is the optimal alignment. These findings suggest that the PPD method is robust and has the ability to accurately identify the number of peaks in noisy signals.

Example 3: Air Quality in California: California is frequently plagued by wildfires that significantly

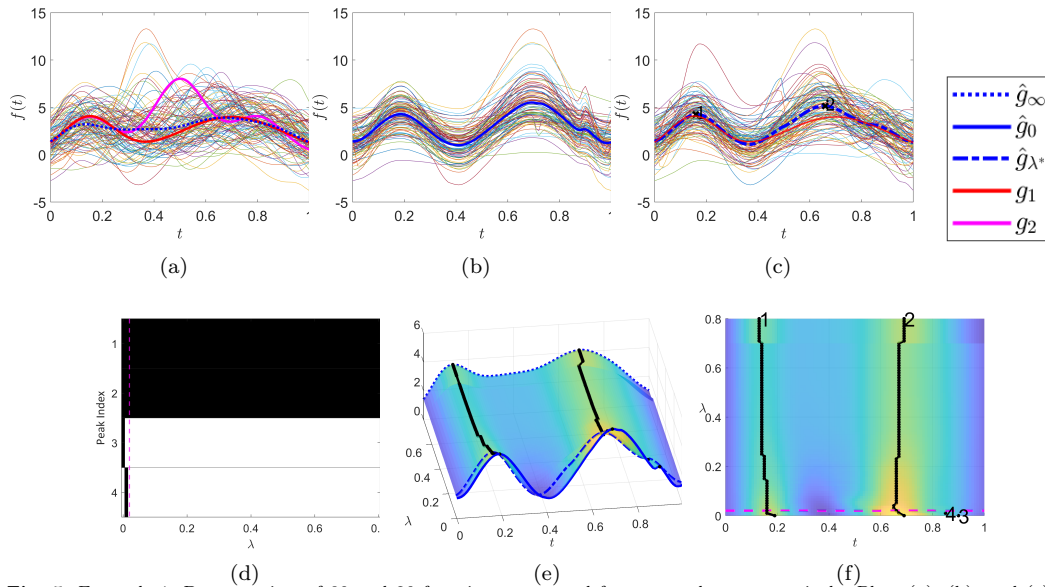


Fig. 5. Example 1: Data consists of 80 and 20 functions generated from g_1 and g_2 , respectively. Plots (a), (b), and (c) display \hat{g}_∞ , \hat{g}_0 , and \hat{g}_{λ^*} . PPDs in (d) through (f) suggest two peaks (1 and 2) are significant and persistent.

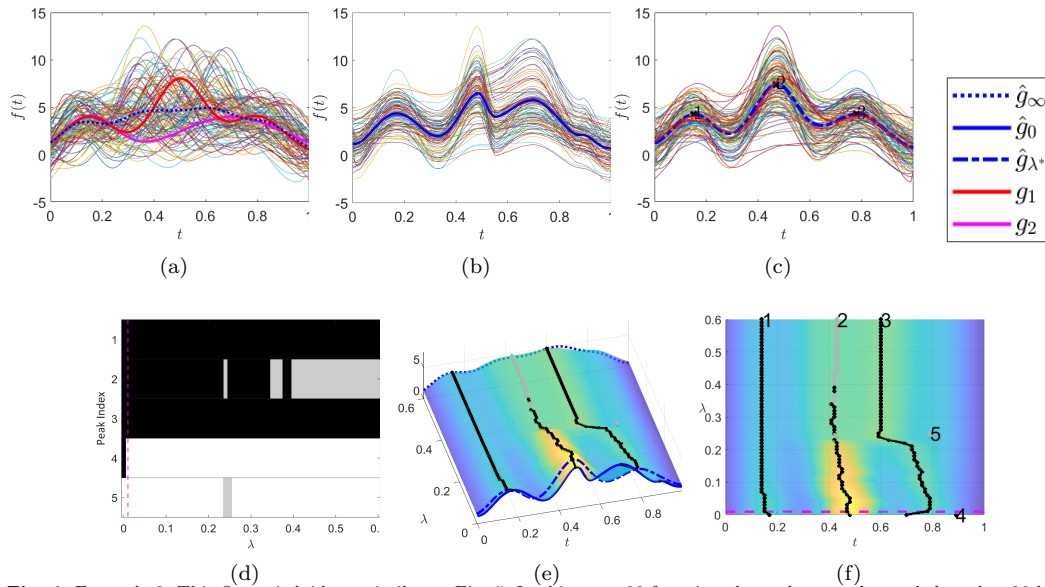


Fig. 6. Example 2: This figure is laid out similar to Fig. 5. In this case, 80 functions have three peaks, and the other 20 have two. PPDs (d) through (f) indicate three peaks (1, 2 and 3) are significant and persistent.

impact its air quality. To study this impact, we analyzed publicly available data from the Environment Protection Agency (EPA) on daily fine particle (PM 2.5) levels in 42 out of 58 counties in California during 2018. Fig. 7 (a) shows the

time-indexed data obtained by smoothing the raw measurements. For smoothing, we employed the *Lowess* (Locally Weighted Scatterplot Smoothing) method with a window size of 50 days. The PPDs in (d), (e), and (f) reveal that the estimated number

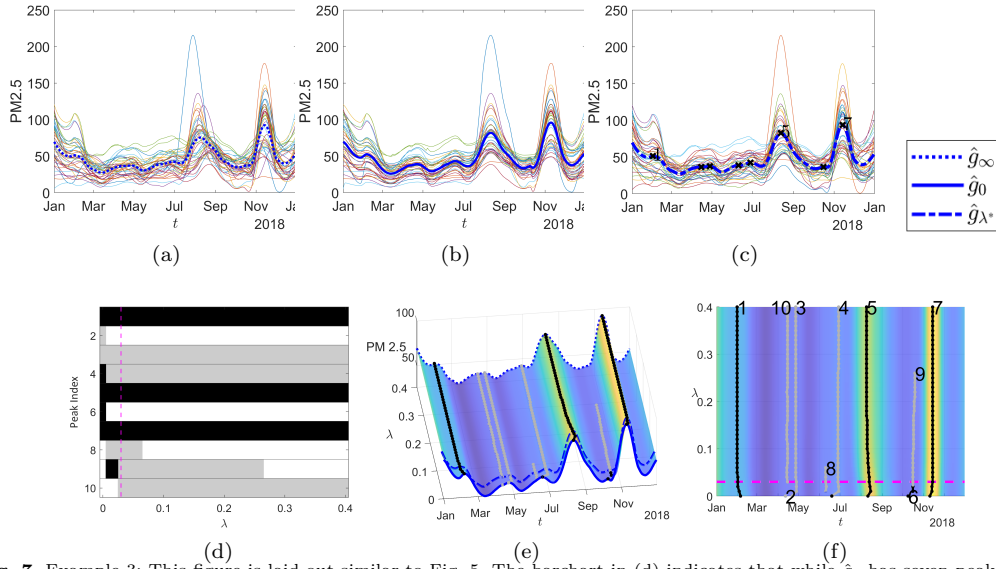


Fig. 7. Example 3: This figure is laid out similar to Fig. 5. The barchart in (d) indicates that while \hat{g}_0 has seven peaks, but only three peaks (1, 5, and 7) are significant and persistent.

of peaks in the ground truth signal, g , is three (1, 5, and 7) with $\lambda^* = 0.03$. In addition to Dec-Jan (the boundaries), the internal peak periods are around Feb, late Aug, and late Nov. The Feb peak is small but significant, while the other two internal peaks are visibly dominant.

Example 4: Birth Rate Changes in European Countries: We analyze a dataset of historical birth rate changes in 50 European countries from 1950 to 2021, collected by Roser et al. (2013). The response variable here is the yearly change in birth rates, where the birth rate implies count of live births per 1,000 individuals each year. The raw data is first smoothed using a window size of 15 years. The PPD method finds that four peaks are significant and persistent. The optimal parameter for this peak is $\lambda^* = 0.09$. Plot (b) demonstrates that \hat{g}_0 exhibits five peaks, but the fifth peak disappears quickly as the value of λ increases. On the other hand, (a) and (d) show that \hat{g}_∞ has four peaks. However, (c) shows \hat{g}_{λ^*} with four significant peaks, namely peak numbers 1 through 4.

Example 5: Consumer Confidence Index of OECD Countries: This example analyzes the monthly consumer confidence index (CCI) of 38 OECD countries from 2008 to 2022, made public by the Organisation for Economic Co-operation and Development (OECD). The CCI is based on surveys of households' financial expectations and economic sentiments. A value above 100 indicates increased confidence and a willingness to spend, while a value below 100 signals pessimism and a tendency to save

more and spend less. As pre-processing, we performed Lowess smoothing method with a window size of 24 months.

Analysis of the dataset using the PPD method, as shown in Fig. 9, reveals that (b) illustrates \hat{g}_0 has four peaks. However, PPDs in plots (d) through (f) suggest that $\lambda^* = 0.04$, with three peaks (1, 2, and 3) identified as significant in \hat{g}_{λ^*} in (c).

Step 2: Peak-constrained Curve Estimation

The next step involves estimating g by utilizing a pre-defined shape class and employing a penalized maximum-likelihood criterion. The objective here is to limit the exploration to the desired shape class and determine the optimal element of that class through geometric search. This technique is an adaptation of the shape-constrained density estimation method suggested in Dasgupta et al. (2021) and has been customized for the functional estimation problem. It involves altering an initial estimate \hat{g}_{init} while simultaneously maximizing a penalized log-likelihood function. (We use the peaks and valleys, including locations and heights, in \hat{g}_{λ^*} and smooth interpolations between them to form an initial estimate, \hat{g}_{init} .) The optimization is conducted across the complete range of functions having the designated shape.

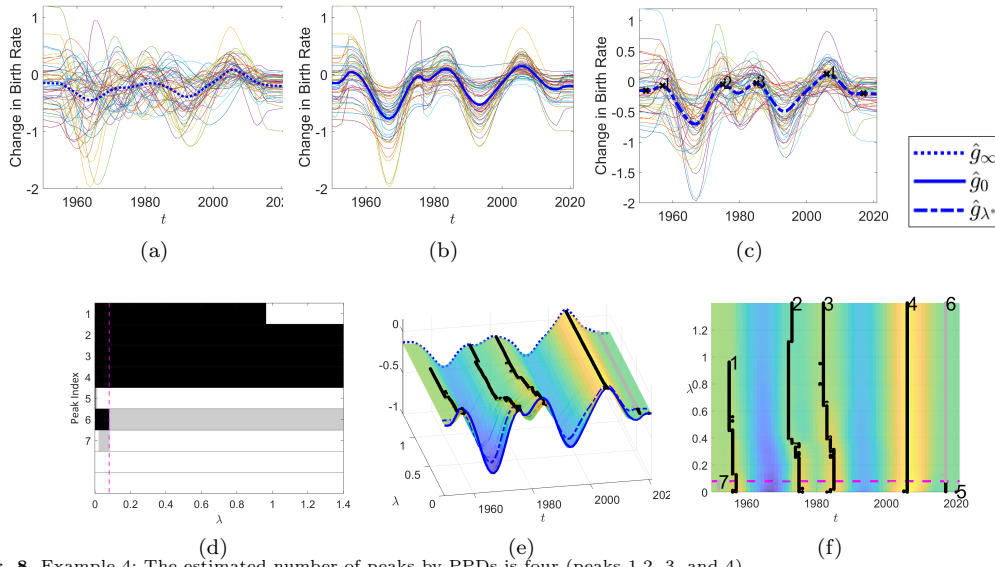


Fig. 8. Example 4: The estimated number of peaks by PPDs is four (peaks 1,2, 3, and 4).

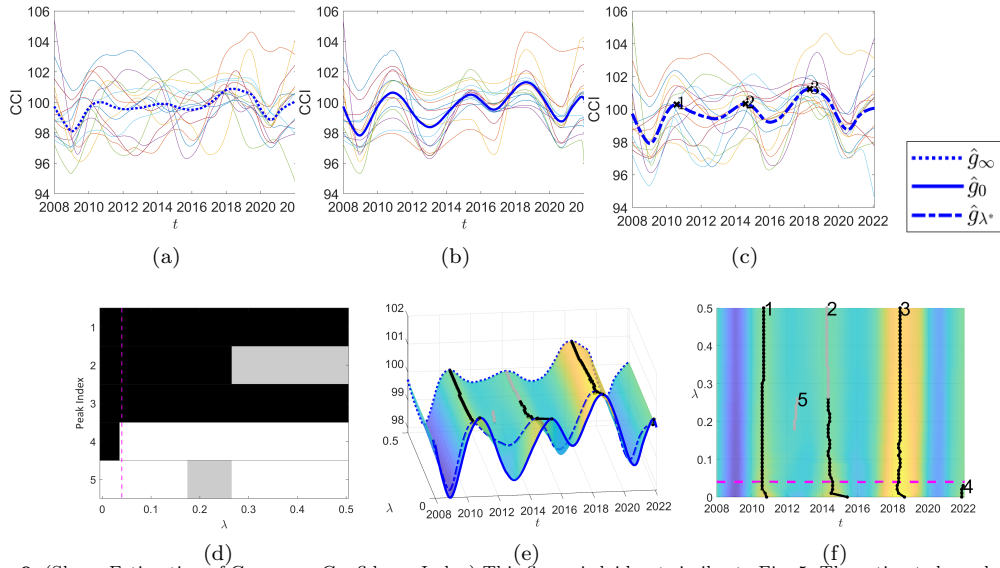


Fig. 9. (Shape Estimation of Consumer Confidence Index) This figure is laid out similar to Fig. 5. The estimated number of peaks by PPDs is three (1, 2, and 3).

Penalized-MLE Approach

Let M be the number of *extrema points* of \hat{g}_{init} , which comprises interior peaks, valleys, and the two endpoints. M lies between $2m+1$ to $2m+3$ (inclusive), where m is the estimated number of interior peaks. For instance, if both endpoints are minima and there

are $m - 1$ interior valleys, then M equals $2m + 1$.

Set of Shape-Constrained Functions: Let a function f have M extrema points in I . We define $\mathcal{F}_m \subset \mathcal{F}$ as the set of all functions with m internal peaks on I . Any two elements of \mathcal{F}_m differ in the locations and heights of their extrema points.

Correspondingly, we are going to define two sets of variables.

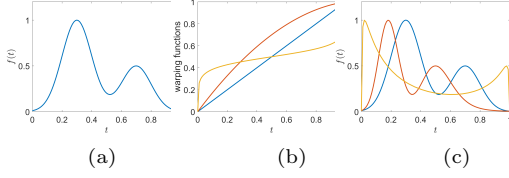


Fig. 10. Time-warping of functions. (a) is the original function, (b) shows three warping functions, (c) is the function warped by corresponding γ 's in (b).

- **Locations:** We will use the time-warping functions – elements of Γ – to vary the location of the extrema points. That is, the composition: $\hat{g}_{init} \circ \gamma$, for a $\gamma \in \Gamma$, changes the locations of the extrema points while maintaining their height and order. Fig. 10 illustrates how the number and the heights of the peaks of a function are invariant to time-warping.
- **Heights:** We also define $\mathbf{s} = \{s_1, s_2, \dots, s_M\}$ as the heights of the extremal points in \hat{g}_{init} . There are some natural constraints on the values of \mathbf{s} . A valley's height should be less than the heights of its neighboring peaks. Let \mathcal{S} be the set of all vectors \mathbf{s} that satisfy these constraints. We will use $f_{\mathbf{s}} \in \mathcal{F}_m$ to denote a function that has \mathbf{s} as the height vector of its extrema.

Starting with the initial estimate \hat{g}_{init} , we adjust the locations and the heights of the extrema points in order to explore the set \mathcal{F}_m . The final estimate is given by: $\hat{g} = (f_{\mathbf{s}^*} \circ \gamma^*)$, where

$$(\gamma^*, \mathbf{s}^*) = \underset{\gamma \in \Gamma, \mathbf{s} \in \mathcal{S}}{\operatorname{argmin}} \left(\sum_{i=1}^n \int_0^1 (f_{\mathbf{s}}(\gamma(t)) - \tilde{f}_{\lambda^*,i}(t))^2 dt + \rho \int_0^1 \ddot{f}_{\mathbf{s}}(\gamma(t))^2 dt \right) \quad (6)$$

Here $\rho > 0$ is an infinitesimal weight ($\sim 10^{-8}$) for favoring smooth functions. This solution differs from Eqn. 4 in several ways. Here we optimize over only one γ while Eqn. 4 uses a γ_i for each observation. Also, we use the partially aligned data that favors m peaks rather than using the original data.

The optimization problem in Eqn. 6 is solved using the `fmincon` function in Matlab. However, since Γ is a nonlinear manifold of infinite dimension, direct optimization poses a challenge. To overcome this, we employ an SRVF map followed by an inverse exponential map to represent the warping functions

in a vector space, and use an orthogonal basis to represent γ by its coefficients. Interested readers can find the optimization details in Dasgupta et al. (2017). Algorithm 2 outlines the steps for shape-constrained estimation of g . Fig. 11 presents an example. In Plot (a), we show partially-aligned functions $\tilde{f}_{\lambda^*,i}$ as dotted points, along with the initial estimate \hat{g}_{init} in cyan color. Plot (b) shows the result of Algorithm 2 in green color. The dark blue line represents the ground truth g .

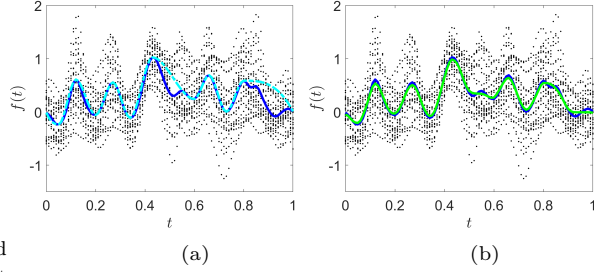


Fig. 11. (Shape Constrained Function Estimation) The dotted points represent the partially-aligned functions $\{\tilde{f}_{\lambda^*,i}\}$ and blue lines are their cross sectional mean. The cyan and the green lines are the initial and final function estimates of g .

Algorithm 2 Peak-constrained Curve Estimation

- Require:** Data: $\{\tilde{f}_{\lambda^*,i}\}_{i=1}^n$, initial shape estimate $\hat{g}_{init}(t)$
- 1: Initialize the heights of the extrema points of \hat{g}_{init} : $\{s_1, s_2, \dots, s_M\}$,
 - 2: Initialize $\gamma \leftarrow \gamma_{id}$.
 - 3: Obtain $\hat{\gamma}$ and $\hat{\mathbf{s}}$ by solving Eqn. 6 by `fmincon`.
 - 4: **return** $\hat{f}(t) = f_{\hat{\gamma},\hat{\mathbf{s}}}(t)$
-

Bootstrapping for Estimating Confidence Bands

To evaluate the performance of the estimate \hat{g} , we compute pointwise confidence bands for our estimator and display them with the estimation results. In the case of simulated data, we check if these estimated confidence bands contain the actual signal and validate our results. Algorithm 3 lays out the steps for computing these confidence bands.

Function Estimator Properties

The basic approach for shape-constrained function estimation follows that presented in Dasgupta et al. (2021), albeit with a different action of the group Γ since that previous paper focused on estimating *pdfs*. The asymptotic properties of the current estimator \hat{g}

Algorithm 3 Constructing Pointwise Functional Confidence Band

Require: $\{f_i\}_{i=1}^n$, Initial shape estimate, \hat{g}_{init} , Estimated smoothing parameter, λ^*

- 1: **for** $j = 1, 2, \dots, B$ **do**
- 2: Resample n functions with replacement to obtain a bootstrapped set of functions, $\{f_i^{(j)}\}_{i=1}^n$.
- 3: Obtain partially aligned functions with smoothing parameter, λ^* , $\{\tilde{f}_{\lambda^*, i}^{(j)}\}_{i=1}^n$
- 4: Given \hat{g}_{init} and $\{\tilde{f}_{\lambda^*, i}^{(j)}\}_{i=1}^n$, obtain the best estimate of g by Algorithm 2: $\hat{g}^{(j)}$
- 5: **end for**
- 6: With $\{\hat{g}^{(j)}\}_{j=1}^B$, **return** $(\alpha/2)$ and $(1 - \alpha/2)$ quantiles to set the lower and upper bound of the confidence bound point-wisely.

remain similar to that of earlier work, and we refer the reader to that paper for details.

Experimental Results: Function Estimation

This section evaluates the performance of our proposed method using a range of simulated and real datasets. The goal is to compare our estimate \hat{g} with two prior solutions, which include: (1) the mean of unaligned functions, $\bar{f} = \hat{g}_\infty$, and (2) the fully-elastic mean, \hat{g}_0 . In addition, we study the results obtained using Eqn. 4 in the case of simulated data. However, due to the unknown optimal κ value (as discussed in Section 2), we present results for several κ values. We use RMSE as the metric for comparing the estimation errors and provide 95% pointwise bootstrap confidence bands to visualize the variability of our estimator.

Simulation Studies

We try four different simulation scenarios on the domain $I = [0, 1]$. In each experiment, we choose a different g and generate $n = 100$ samples according to Eqn. 3. To compute and compare different solutions, we use 50 independent simulations of each scenario and compute statistics of RMSEs of the estimators.

- **Simulated Dataset 1**

Fig. 12 shows results from experiments on the first dataset. The original data is shown in panel (a), with the true function g drawn in red. Plots (a) and (b) show the alignment of functions under the extreme values of λ : ∞ and 0, respectively. The cross-sectional means are shown in blue in each case. The PPD bar chart for this data is shown in (d), which estimates two significant internal peaks. The optimal parameter $\lambda^* = 0.05$ is shown in the magenta, dotted vertical line in (d). Plots (e) and (f) are PPD surfaces

displaying gradual changes in \hat{g}_λ when λ increases. The black lines on this surface are traces of significant peaks. Plot (f) shows the top view of the surface. For this λ^* , (c) shows the partially aligned functions, $\{\tilde{f}_{\lambda^*, i}\}_{i=1}^n$ (as a point cloud to help visibility). Their mean \hat{g}_{λ^*} is shown using a dotted-line blue curve and captures the geometric features of g better than \hat{g}_0 and \hat{g}_∞ . The dashed cyan line is the initial estimate, \hat{g}_{init} .

Next we use these quantities to estimate g as described in Section 5. The green dashed curve in (g) is the final estimate \hat{g} . We also display a pointwise bootstrap confidence band using a gray region. We can see that both the function estimate (in green) and the band (in gray) are distinguishable from \hat{g}_0 and \hat{g}_∞ over large intervals. Furthermore, \hat{g} is the closest function to the ground truth g in terms of the \mathbb{L}^2 distance. A detailed quantitative evaluation of the results is presented later.

- **Simulated Dataset 2**

This experiment uses a sawtooth wave function for g , and the data is shown in Fig. 13 (a). The rest of this figure is laid out similarly to Fig. 12. The PPD bar chart in Plot (d) successfully detects two significant internal peaks, labeled 3 and 6, and estimates $\lambda^* = 0.04$. The evolution of peaks is seen in (e) and (f) with PPD surface plots. Plot (c) shows the partially-aligned functions, $\{\tilde{f}_{\lambda^*, i}\}_{i=1}^n$, their mean, \hat{g}_{λ^*} , and the initial estimate, \hat{g}_{init} at $\lambda^* = 0.04$. Plot (g) shows the final estimate \hat{g} (in green) with a bootstrap confidence band in gray. As shown, the elastic mean, \hat{g}_0 (solid blue), has spurious peaks while \hat{g}_∞ (dotted blue) underestimates the heights of peaks and valleys. Our estimate \hat{g} (in green) provides an excellent estimate of g .

- **Simulated Dataset 3**

In this case, we select a function g with two peaks and a large constant region in between peaks. The constant interval is difficult to estimate as noise can erroneously introduce spurious peaks in a flat region, as shown in Plot (b) of Fig. 14. This data has some short-lived peaks and others that do not pass the significance test. The PPD bar chart detects peaks 2 and 5 as significant and persistent, with the resulting $\lambda^* = 0.03$. The PPD surface plots in (e) and (f) show the evolution of these peaks. Plot (g) presents the final estimate (green) with a point-wise confidence band (gray) which is considerably different from \hat{g}_0 (solid blue) and \hat{g}_∞ (dotted blue).

- **Simulated Dataset 4**

In this example, we use a broad unimodal function with moderate slope and large phase variability in the

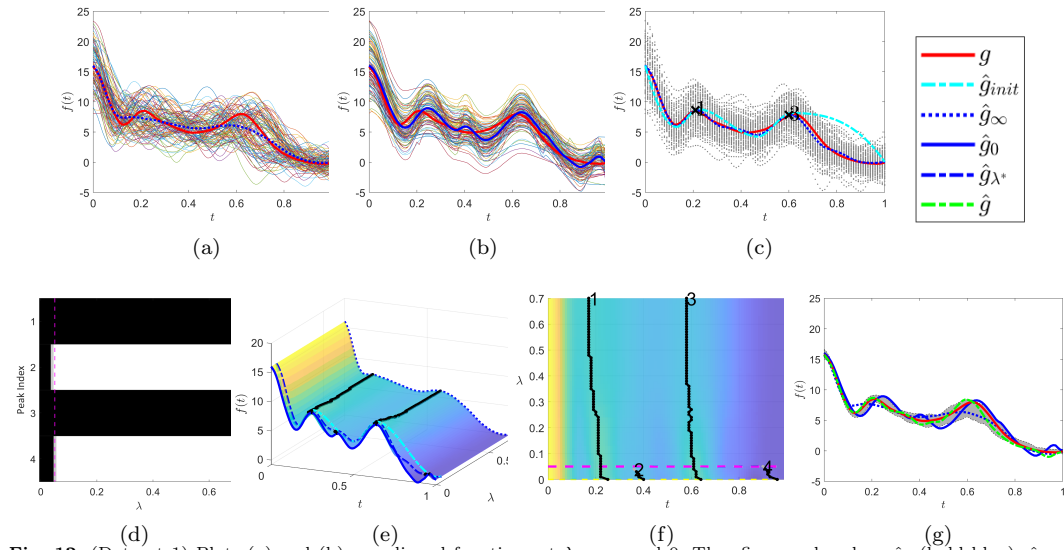


Fig. 12. (Dataset 1) Plots (a) and (b) are aligned functions at $\lambda = \infty$ and 0. These figures also show \hat{g}_0 (bold blue), $\hat{g}_{0.05}$ (bold dotted-line blue) and \hat{g}_∞ (bold dotted blue). The ground truth g , initial estimate \hat{g}_{init} , and the final estimate \hat{g} are drawn in red, cyan, and green, respectively. Plot (d) is the PPD, with $\lambda^* = 0.05$. Plot (e) and (f) show the evolution of \hat{g}_λ versus λ . The black lines on the surface indicate the interior peaks, and (f) is the top view of (e). Plot (c) contains the aligned functions at λ^* . Panel (g) compares the unaligned mean, fully elastic mean, our estimate, and the ground truth, g . A 95% bootstrap confidence band is drawn using gray regions.

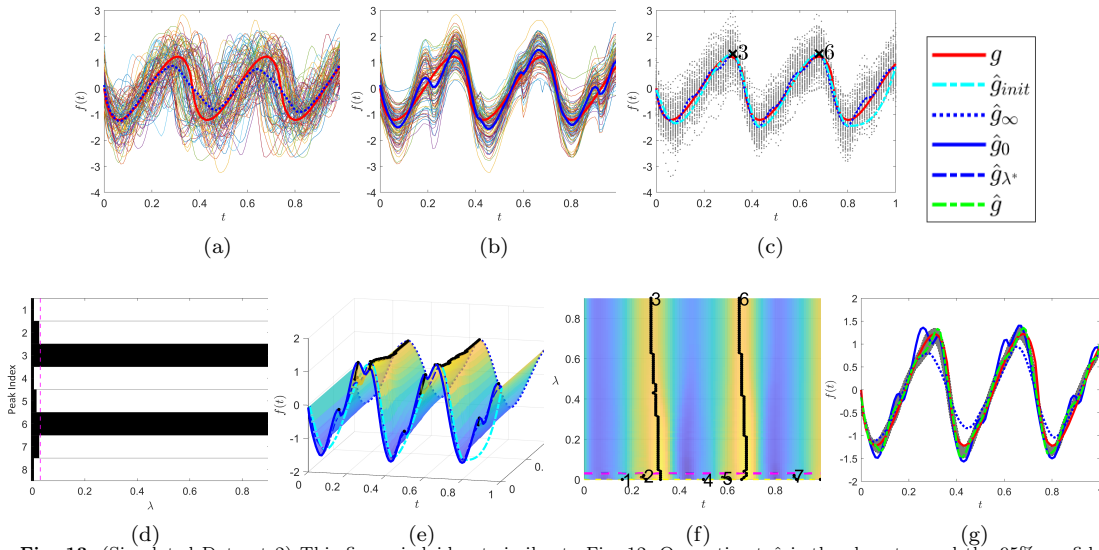


Fig. 13. (Simulated Dataset 2) This figure is laid out similar to Fig. 12. Our estimate \hat{g} is the closest g and the 95% confidence band contains g entirely.

data. Fig. 15 (a) shows the original data. The PPD barchart in (d) successfully screens spurious peaks at $\lambda^* = 0.11$. Plot (g) displays the final estimate, \hat{g} . We

find that \hat{g} provides a good estimate by capturing the location and the height of the peak of g .

- *Quantification of Estimation Performance*

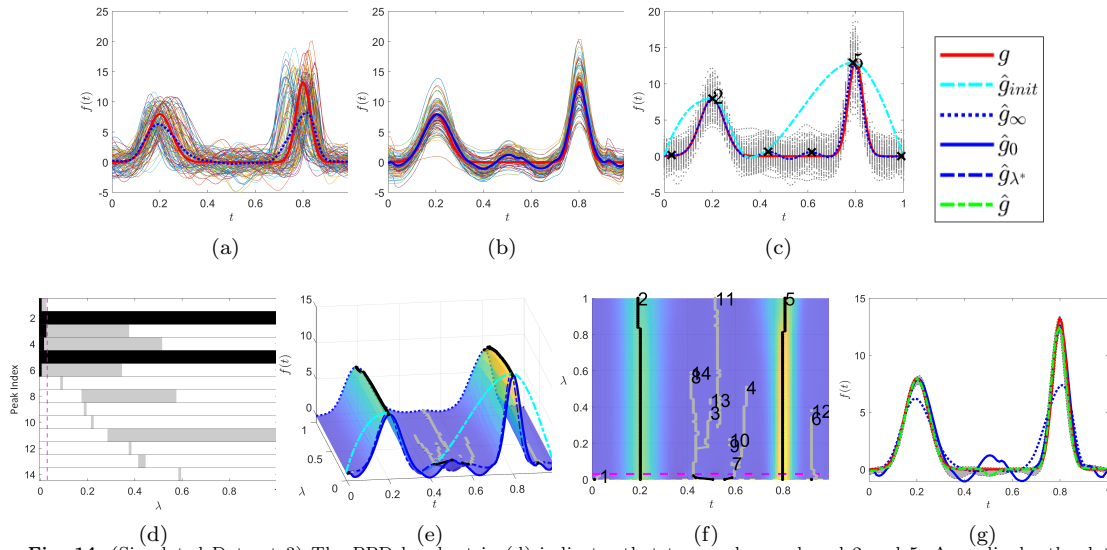


Fig. 14. (Simulated Dataset 3) The PPD barchart in (d) indicates that two peaks numbered 2 and 5. Accordingly, the dotted cyan lines in (c) and (e) are the estimated shape of g . The final estimate \hat{g} is shown in (g).

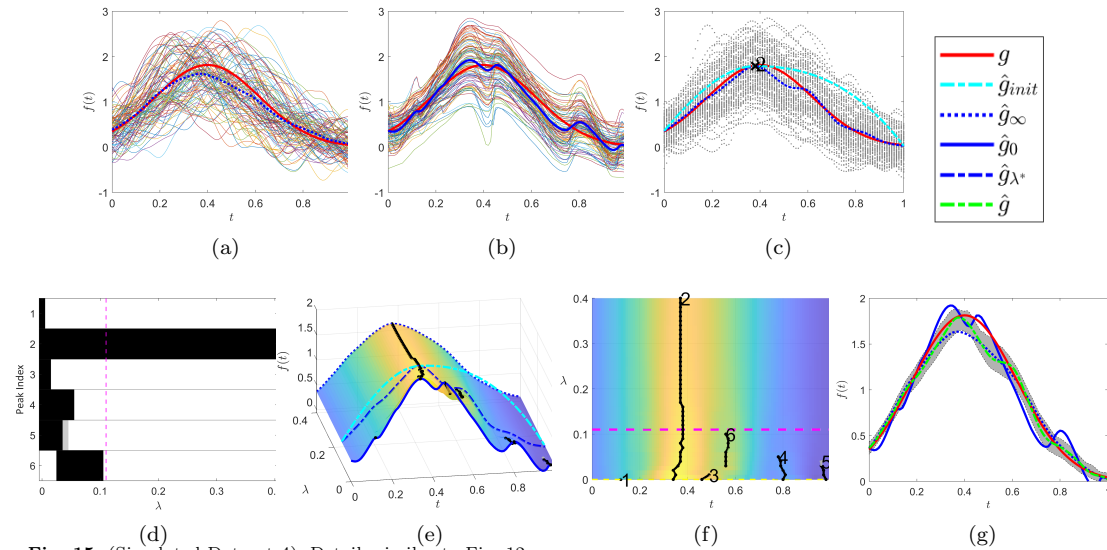


Fig. 15. (Simulated Dataset 4): Details similar to Fig. 12.

So far we have pictorially analyzed estimates from different methods. To quantify accuracy of these estimates, we conduct 50 replications of each experiment and calculated the estimation errors. Fig. 16 displays boxplots of the mean and standard deviations of the L^2 errors for the four simulation experiments. It shows that \hat{g} , the third box in the boxplot, provides the lowest RMSE. In comparisons, the unaligned mean (\hat{g}_∞) fails poorly in estimating

the heights of peaks and valleys, and the fully aligned mean (\hat{g}_0) overestimates the number of peaks. To emphasize the role of shape in estimation, Fig. 17 shows the histograms of the estimated number of peaks for different simulation datasets. The upper row histograms the number of peaks in the cross-sectional mean of the partially aligned mean, \hat{g}_{λ^*} . These include both significant and insignificant peaks. The bottom row shows histograms of the number

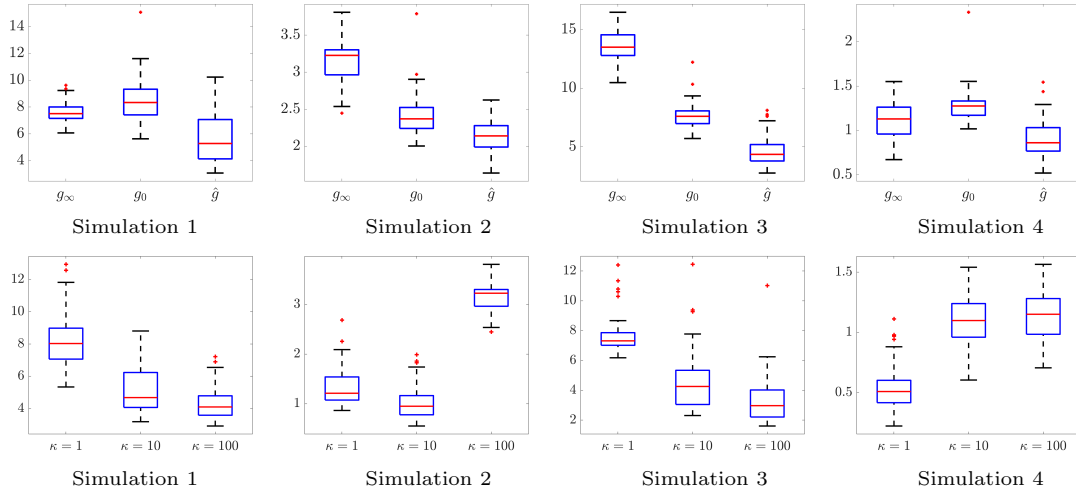


Fig. 16. Top: The boxplots of the L^2 errors of three different estimators on four simulation scenarios. Bottom: The boxplots for the penalized- L^2 estimators for different values of κ .

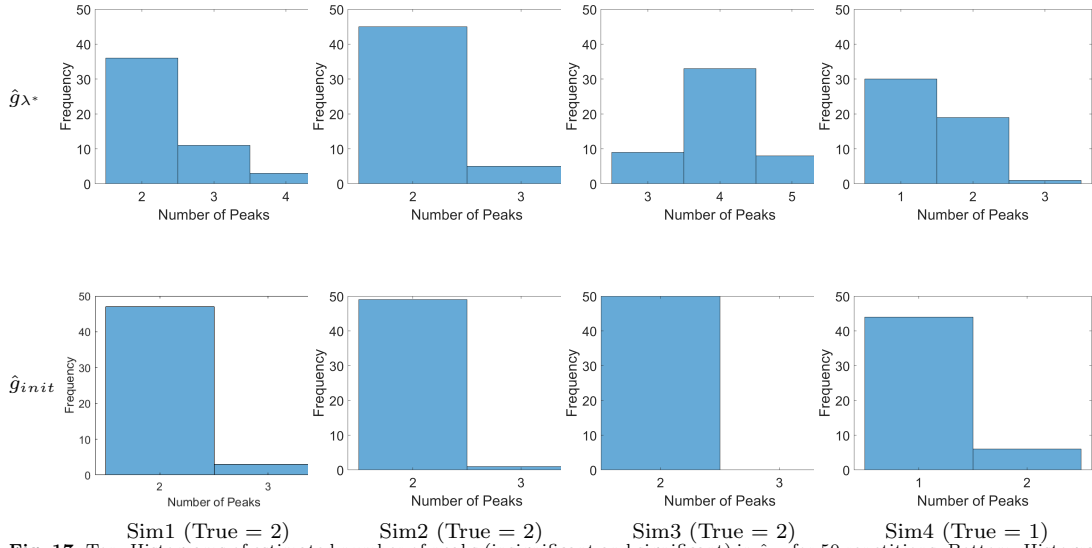


Fig. 17. Top: Histograms of estimated number of peaks (insignificant and significant) in \hat{g}_{λ^*} for 50 repetitions. Bottom: Histograms of numbers of significant peaks estimated using PPD.

of the significant peaks selected by PPD. As these results show, the PPD approach is able to estimate the correct number of peaks in g most of the time. This contributes to the improved performance of the proposed shape-constrained function estimator.

Finally, we analyze the computational cost of our estimation procedure relative to the past methods. Table 1 lists the time to perform different algorithmic steps. This cost is computed on a CPU (Intel(R)) i7-11800H @ 2.30GHz. We omit the cost of unaligned

mean as it does not require any functional alignment. The cost for computing the fully elastic mean averaged over 50 replications is in the first column. Lastly, the costs of different steps of our method – costs for partial alignment, computing PPD, and function estimation – are listed in the three right columns. Most of the time is consumed in the partial alignment of functions for different values of λ .

Table 1. Computational time (in seconds) for various steps in our procedure.

	Fully Elastic	Partial Alignment		
	Aligning Functions	Aligning Functions (1st Step)	Computing PPDs (1st Step)	Function Estimation (2nd Step)
Simulation 1	15.29	1868.4	0.13	17.87
Simulation 2	17.12	2021.6	0.12	18.92
Simulation 3	14.59	2205.0	0.14	38.16
Simulation 4	15.83	1564.8	0.09	17.01

Real Data Studies

In this section, we apply our method to estimate functions g underlying some real datasets. However, in these cases, we are unable to compare our estimates to a ground truth function to evaluate their accuracy. Therefore, the results must be interpreted and compared to other estimators in order to assess their performance.

Berkeley Growth Rate Data:

First, we study the classical Berkeley Growth Study data (Ramsay and Silverman (1997)) often used to demonstrate the phase variability in functional data. The female datasets contains the rates of growth in heights of 54 girls from ages 1 to 18. The peaks in growth curves are called the *growth spurts* and of great interest. Scientists and physicians use a growth chart to analyze individual growths and ask the question: How many growth spurts to the individuals (male or female) have on average? What is the average growth profile for a human being in that category? Fig. 18 (a) shows the raw data for female subjects and (b) shows fully aligned functions. The unaligned mean (blue curve in (a)) smooths out almost all the growth spurts and can be a bad representative of the population. The full aligned mean (blue curve in (b)) shows several strong spurts but also some relatively weak spurts. Among the 13 peaks generated, the PPD chart selects four internal peaks (2, 3, 5, and 8) as significant and persistent, concluding that female growth has three main growth spurts. The plot on (g) shows the estimated function \hat{g} in green color.

COVID-19 Data Analysis for Europe

There is a great interest in analyzing COVID pandemic data and associated surges in infection rates. While different communities experienced COVID peaks (or waves) at asynchronous times, there are common patterns underlying COVID incidences and outcomes. For instance, if we focus on COVID outcomes for different countries in the region, there is arguably an overall pattern of waves during the pandemic period.

- Daily Hospitalization Rate Curves:** We consider the daily hospital-occupancy counts associated with COVID-19 in 25 European countries during the period from April 2020 to July 2021 (Mathieu et al. (2020)). Fig. 19 (a) and (b) display the functional data for infection rates and fully-aligned functions with their means, \hat{g}_∞ and \hat{g}_0 , respectively. As shown, \hat{g}_∞ and \hat{g}_0 differ a lot in terms of the shapes and the heights of peaks. PPD surface plots in (e) and (f) show the gradual changes in \hat{g}_λ with respect to $\lambda \in [0, 0.2]$, and the barchart in (d) selects $\lambda^* = 0.025$ with three persistent peaks (1, 4 and 6). Our final estimate (in green) in panel (g) highlights this estimated shape. The 95% pointwise bootstrapped confidence band (in gray) in (g) has a wide range, and this can be attributed to a small sample size $n = 25$.
- Daily Infection Rate Curves:** The daily infection rate curves of COVID-19 can be used to study rate of spread of a variant or the effectiveness of a vaccine. We collected the infection rate curves in 25 European countries from OWID (Mathieu et al. (2020)) for the period April 2020 to March 2022. Fig. 20 (a) and (b) show the functional data and the fully-aligned functions, respectively. Although the functions in (b) are well aligned, some of the peaks in the first half of I appear weak. Indeed, the PPD method rejects all peaks prior to July 2021 as insignificant and keeps only three later peaks. Plot (g) shows our final estimate (in green) and it shows a long flat region in the first half. This suggests that significant waves occurred during the outbreak of the delta variant in the Fall 2021. It also discovers a prominent peak around January 2022, which is not present in \hat{g}_∞ .
- Daily Death Rate Curves:** We also studied the daily death rates of COVID in these 25 European countries for April 2020 to March 2022. The standard estimates \hat{g}_∞ (dotted blue) and \hat{g}_0 (solid blue) in Fig. 21 (a) and (b) differ considerably: \hat{g}_0 has several prominent peaks whereas \hat{g}_∞ has

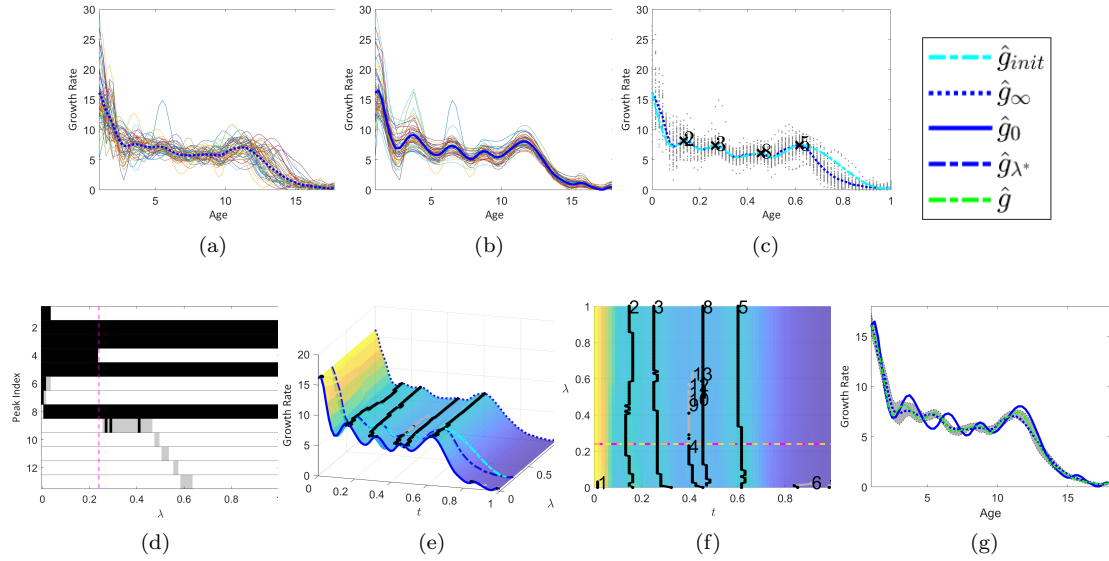


Fig. 18. (Female Growth Rate Data) Unaligned raw data is in (a), and fully-elastic alignment is in (b). PPD in (d) denotes that five peaks (2, 3, 5, and 8) are persistent. (c) shows the partially aligned point cloud and initial shape estimate of g (cyan curve). Plots (e) and (f) demonstrate the gradual changes of aligned functions and their peak process behaviors as λ increases. (g) shows the estimate underlying function.

fewer. Specifically, the peak around January 2021 in \hat{g}_0 seems artificial as no country has a peak in the original data, and there is no reason to align the peak at the specific time. The PPDs in (d), (e), and (f) estimate $\lambda^* = 0.025$ and the peak labeled 4 disappears as λ increases. As shown in Plot (g), the final estimation, \hat{g} (in green), is different from both \hat{g}_∞ and \hat{g}_0 . Although the partial alignment of functions is not too different from the original data, our estimate \hat{g} picks up three distinct peaks in the early stage of COVID before January 2021.

Household Electricity Consumption Data

The objective of next experiment is to analyze the half-hourly electricity consumption data in domestic households in a specific neighborhood in Tallahassee, FL Dasgupta et al. (2019). This study focuses on two subsets of the data, corresponding to the months of January and July, consisting of 968 and 1,219 functions, respectively. Fig. 22 (a) and (b) present the original and aligned functions of the January data. The PPD barchart reveals that five peaks (5, 7, 10, 11, and 12) are significant, with $\lambda^* = 0.245$. Panel (g) shows that there are vast differences among different estimators: \hat{g} (in green), \hat{g}_0 (in solid blue), and \hat{g}_∞ (in dotted blue). Figure 23 presents results for the July subset. The PPD barchart reveals two prominent peaks (2 and 5) with $\lambda^* = 0.18$, while g_0 and g_∞ suggest three and one peaks, respectively.

Discussion

The experimental results presented in this paper provide evidence that our approach is successful in: (1) estimating the number of peaks in functional data, and (2) estimating the underlying unknown function in a shape constrained manner. An important accomplishment here is the automated selection of the tuning parameter λ using PPDs. The use of PPD is not only intuitive but also effective in determining the number and locations of peaks in g , allowing for the selection of a reasonable value for the smoothing parameter, λ . Moreover, shape-constrained functional estimation refines the estimate, \hat{g} , by eliminating insignificant peaks as determined by PPD.

An pertinent question here is: Why not define the concept of PPDs in the original function space, why use the SRVF representation instead? Fig. 24 illustrates as example to answer this question. It tries to form a PPD on one of the previously studied simulated data, and concludes that $\kappa = 0$ is optimal. This, of course, is incorrect as the pinching effect is clearly visible at $\kappa = 0$. Under the SRVF representation, the pinching effect is completely avoided, even for $\lambda = 0$.

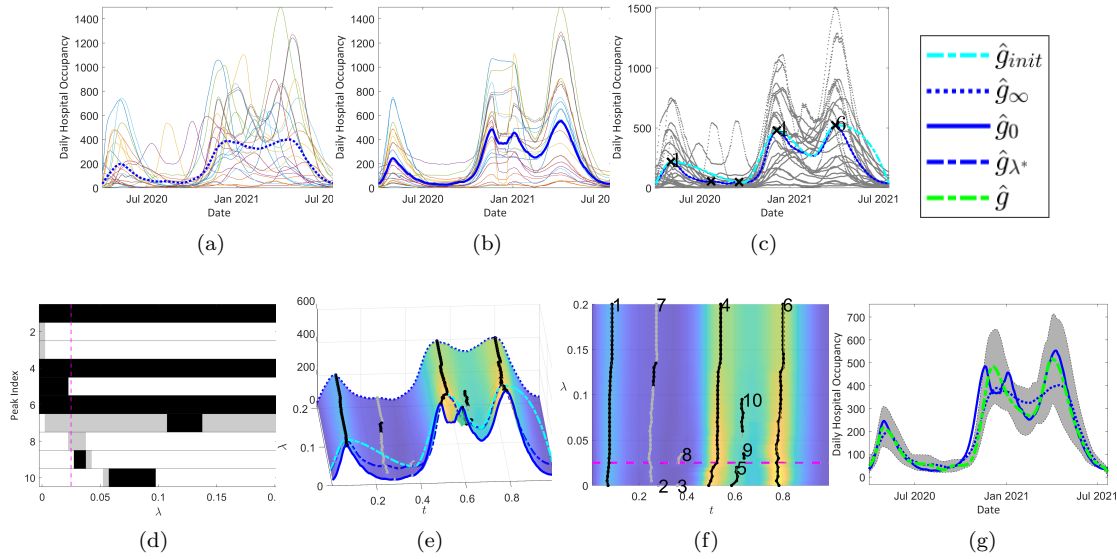


Fig. 19. (Daily Hospital Occupancy in Europe) PPD in (d) suggests that three peaks (1,4 and 6) are real features of the ground truth. In Plot (b), four peaks exist, and peak number 5 is a notable difference between \hat{g}_∞ and \hat{g}_0 . With $\lambda^* = 0.025$ from (d), the final estimation (in green) in Plot (g) is distinguishable with the others, \hat{g}_∞ and \hat{g}_0 . The 95% bootstrapped confidence band seems wide due to the small sample size.

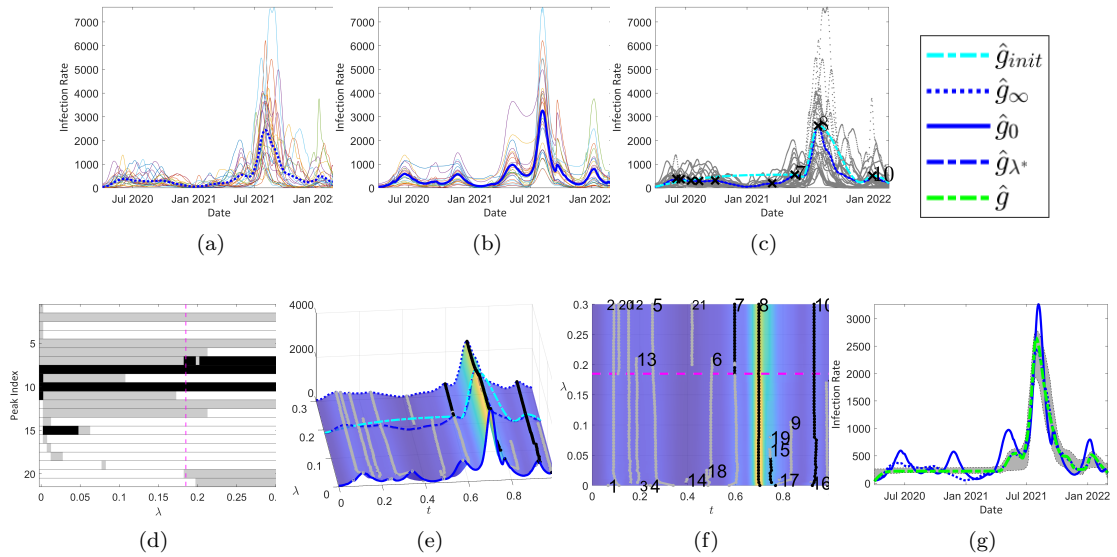


Fig. 20. (Daily Infection Rate in Europe) PPD in (d) labels three peaks (7, 8, and 10) as significant. Our final estimation (green curve in (g)) removes all small peaks in the early stages and select the three most persistent waves.

Conclusion & Future Work

Understanding the population behavior of the sampled functional data requires estimating the actual underlying signal g . In many cases, the number,

locations, or heights of extrema can be of direct interest themselves. In the presence of phase and additive noise, the classical unaligned mean \hat{g}_∞ loses the geometric characteristics of g , while fully elastic mean \hat{g}_0 generates spurious peaks. This paper

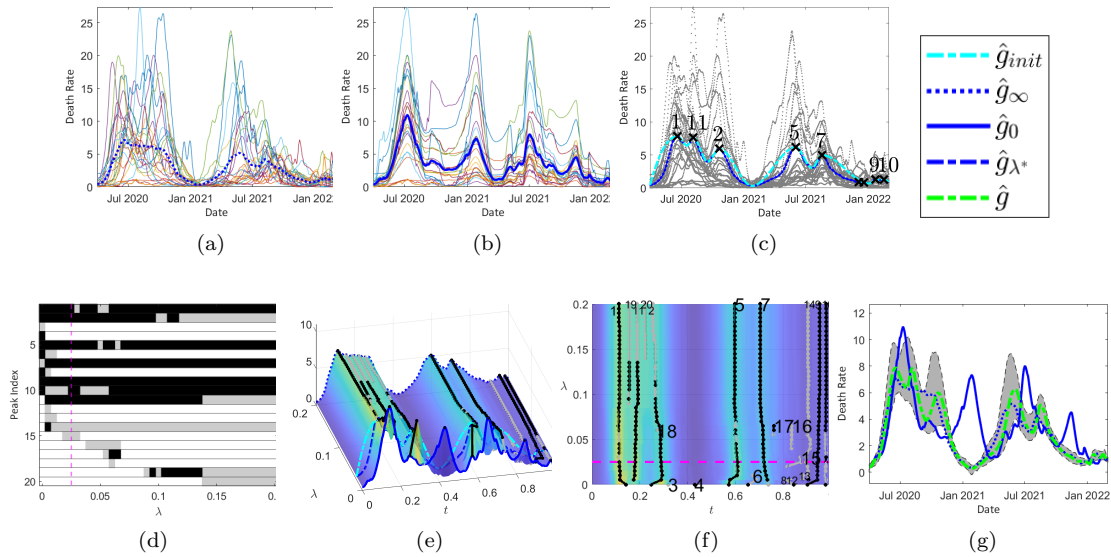


Fig. 21. (Death Rate in Europe) PPD in (d) suggests that seven peaks (1, 2, 5, 7, 9, 10, and 11) are significant. Our final estimation (green curve in (g)) indicates five major peaks and two minor ones with a big valley in the middle.

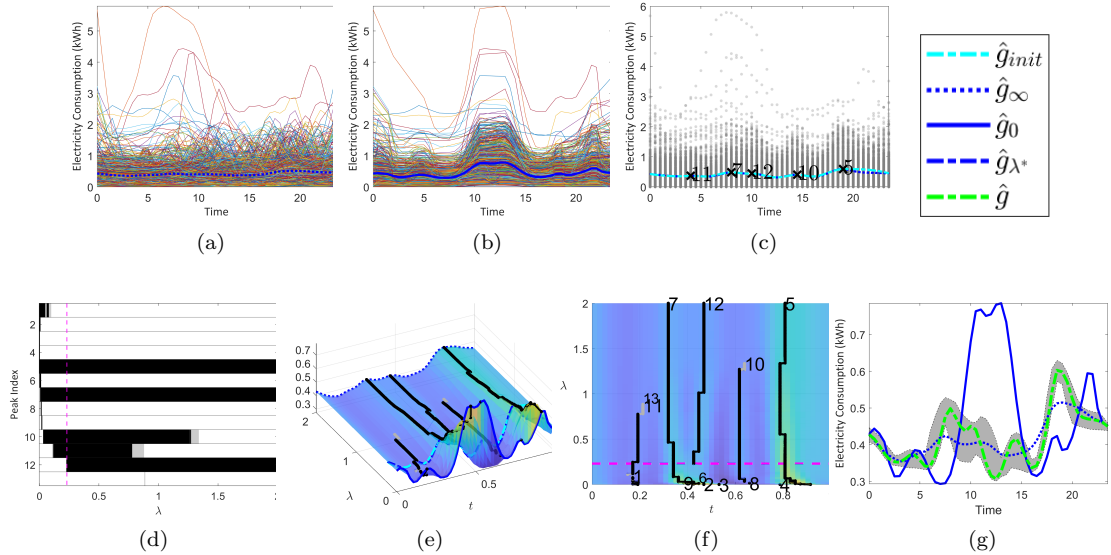


Fig. 22. (Electric Consumption in Tallahassee, FL, in January 2015) Plots (a) and (b) show household data and fully-aligned functions, respectively. PPD in (d) provides $\lambda^* = 0.235$, and five significant peaks (5, 7, 10, 11, 12). The final estimation, \hat{g} , (in green) in (g), is distinctive from the others, \hat{g}_∞ , and \hat{g}_0 .

presents a geometric approach that estimates the shape features and the graph of function g . This approach explores the solution space by studying geometry of \hat{g}_λ , for a range of smoothing parameter $\lambda \in [0, \infty)$. It introduces a novel tool called peak persistence diagram (PPD) for investigating

this geometric space and for focusing on persistent peaks. This persistence of peaks helps us to discard insignificant peaks, estimate the shape of g and reach an optimal λ^* . The latter two quantities lead to a shape-constrained estimation of g . This estimation refines \hat{g}_{λ^*} and produces an optimal estimate, \hat{g}

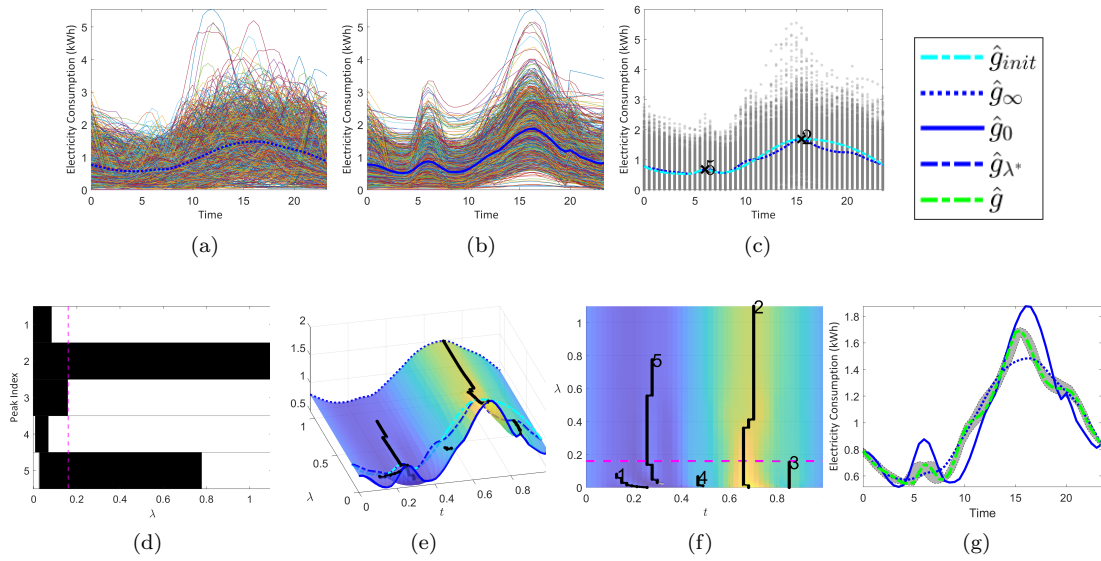


Fig. 23. (Electric Consumption in Tallahassee in July 2015) Plots (a) and (b) illustrate original data and fully-aligned functions, respectively. PPD in (d) provides $\lambda^* = 0.18$, and two significant peaks (2, 5). The final estimation, \hat{g} , (in green) in (g), is distinctive from the others, \hat{g}_∞ , and \hat{g}_0 .

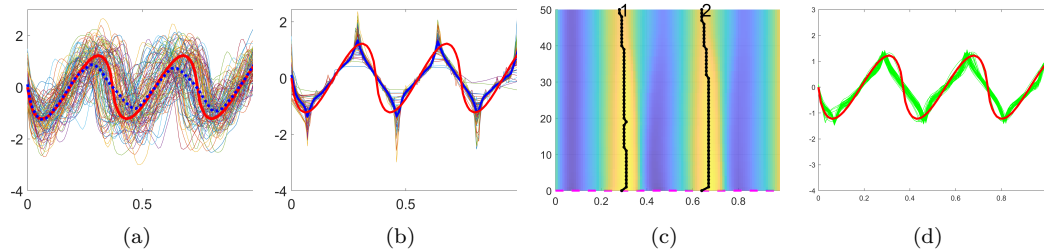


Fig. 24. (PPD on for \hat{g}_{L2}) Panel (a) displays the raw functions with the cross-sectional mean (in dotted blue) and \hat{g}_{L2} (in red). Panel (b) shows the alignment of the functions using L^2 metric with its mean (in blue) when $\kappa = 0$. Panel (c) displays the posterior probability density (PPD) plot, which suggests that $\kappa = 0$ is the optimal value. Panel (d) presents the results of 50 replicated simulations with the estimates, \hat{g}_{L2} , plotted in green.

under penalized MLE. Most importantly, the heights, the locations, and the number of extrema in \hat{g} are interpretable and supported by data. In contrast, \hat{g}_∞ underestimates the peak heights, and \hat{g}_0 overestimates heights as well as the number of extrema.

As a follow-up study, we are interested in separating the trend and the seasonality of the true underlying signal, i.e., $f_i(t) = g_1(t) + (g_2 \circ \gamma_i)(t) + \epsilon_i(t)$ where g_1 and g_2 are trend and seasonality functions with time-warping, $\{\gamma_i\}$, and additive noise, $\{\epsilon_i\}$. Separating the data into two main signals may allow one to take a deeper look at it. For example, when investigating climate change datasets such as CO_2 emissions or global temperatures, one can expect a trend, g_1 , with seasonal volatility, g_2 . By separating

the trend from the seasonality, one can test the trends statistically. In another direction, we can extend our assumption that there exists a single true source. For instance, in real-world settings, it is difficult to ascertain if the sampled functions, $\{f_i\}$, were generated from a single signal g .

References

- Allasonnière, S., Amit, Y. and Trouvé, A. (2007) Towards a coherent statistical framework for dense deformable template estimation. *Journal of the Royal Statistical Society (B)*, **69**, 3–29.
- Chaudhuri, P. and Marron, J. S. (1999) Sizer for exploration of structures in curves. *Journal of the*

- American Statistical Association*, **94**, 807–823.
- Cheng, M.-Y., Gasser, T. and Hall, P. (1999) Nonparametric density estimation under unimodality and monotonicity constraints. *J. Comput. Graph. Stat.*, **8**, 1–21.
- Cheng, W., Dryden, I. and Huang, X. (2013) Bayesian registration of functions and curves. *Bayesian Analysis*, **2015**.
- Choudhuri, N., Ghosal, S. and Roy, A. (2005) Bayesian methods for function estimation. In *Bayesian Thinking* (eds. D. Dey and C. Rao), vol. 25 of *Handbook of Statistics*, 373–414. Elsevier.
- Claeskens, G., Devijver, E. and Gijbels, I. (2021) Nonlinear mixed effects modeling and warping for functional data using b-splines. *Electronic Journal of Statistics*, **15**.
- Dasgupta, S., Pati, D., Jermyn, I. H. and Srivastava, A. (2021) Modality-constrained density estimation via deformable templates. *Technometrics*, **63**, 536–547.
- Dasgupta, S., Pati, D. and Srivastava, A. (2017) A two-step geometric framework for density modeling.
- Dasgupta, S., Srivastava, A., Cordova, J. and Arghandeh, R. (2019) Clustering household electrical load profiles using elastic shape analysis. In *2019 IEEE Milan PowerTech*, 1–6.
- Doss, C. R. and Wellner, J. A. (2016) Global rates of convergence of the MLEs of log-concave and S-concave densities. *Annals of Statistics*, **44**, 954–981.
- Earls, C. and Hooker, G. (2017) Variational Bayes for Functional Data Registration, Smoothing, and Prediction. *Bayesian Analysis*, **12**, 557 – 582.
- Fan, J. and Gijbels, I. (1996) *Local polynomial modelling and its applications*. Boca Raton, Fla.: Chapman & Hall/CRC.
- Green, P. and Silverman, B. (1994) *Nonparametric regression and generalized linear models: a roughness penalty approach*. United Kingdom: Chapman and Hall.
- Grenander, U. (1956) On the theory of mortality measurement: part ii. *Scand. Actuar. J.*
- Horton, W., Page, G., Reese, C., Lepley, L. and White, M. (2020) Template priors in bayesian curve registration. *Technometrics*, **63**, 1–13.
- Kneip, A. and Ramsay, J. O. (2008) Combining registration and fitting for functional models. *Journal of American Statistical Association*, **103**.
- Kurtek, S. (2017) A geometric approach to pairwise Bayesian alignment of functional data using importance sampling. *Electronic Journal of Statistics*, **11**, 502 – 531.
- Kurtek, S., Srivastava, A. and Wu, W. (2011) Signal estimation under random time-warpings and nonlinear signal alignment. In *Advances in Neural Information Processing Systems* (eds. J. Shawe-Taylor, R. Zemel, P. Bartlett, F. Pereira and K. Weinberger), vol. 24. Curran Associates, Inc.
- Liu, X. and Muller, H. G. (2004) Functional convex averaging and synchronization for time-warped random curves. *J. American Statistical Association*, **99**, 687–699.
- Lu, Y., Herbei, R. and Kurtek, S. (2017) Bayesian registration of functions with a gaussian process prior. *Journal of Computational and Graphical Statistics*, **26**, 894–904.
- Marron, J. S., Ramsay, J. O., Sangalli, L. M. and Srivastava, A. (2015) Functional data analysis of amplitude and phase variation. *Statistical Science*, 468–484.
- Mathieu, E., Ritchie, H., Rodés-Guirao, L., Appel, C., Giattino, C., Hasell, J., Macdonald, B., Dattani, S., Beltekian, D., Ortiz-Ospina, E. and Roser, M. (2020) Coronavirus pandemic (covid-19). *Our World in Data*.
- Matuk, J., Bharath, K., Chkrebtii, O. and Kurtek, S. (2021) Bayesian framework for simultaneous registration and estimation of noisy, sparse, and fragmented functional data. *Journal of the American Statistical Association*, **0**, 1–17.
- Minnotte, M. C. (1997) Nonparametric testing of the existence of modes. *The Annals of Statistics*, **25**, 1646–1660.
- Raket, L. L., Sommer, S. and Markussen, B. (2014) A nonlinear mixed-effects model for simultaneous smoothing and registration of functional data. *Pattern Recognition Letters*, **38**, 1–7.
- Ramsay, J. and Silverman, B. (1997) *Functional Data Analysis*. Springer series in statistics. Springer.
- Ramsay, J. O. and Li, X. (1998) Curve registration. *Journal of the Royal Statistical Society: Series B (Statistical Methodology)*, **60**, 351–363.
- Roser, M., Ritchie, H., Ortiz-Ospina, E. and Rodés-Guirao, L. (2013) World population growth. *Our World in Data*.
- Samworth, R. J. and Sen, B. (2018) Editorial: Special issue on nonparametric inference under shape constraints. *Statistical Science*, **33**, 469–472.
- Simpson, I. J., Schnabel, J. A., Groves, A. R., Andersson, J. L. and Woolrich, M. W. (2012) Probabilistic inference of regularisation in non-rigid registration. *NeuroImage*, **59**, 2438–2451.
- Srivastava, A. and Klassen, E. (2016) *Functional and Shape Data Analysis*. Springer Series in Statistics. Springer New York.
- Srivastava, A., Wu, W., Kurtek, S., Klassen, E. and Marron, J. S. (2011) Registration of functional data using Fisher-Rao Metric.
- Stöcker, A., Pfeuffer, M., Steyer, L. and Greven, S. (2022) Elastic full procrustes analysis of plane curves via hermitian covariance smoothing.
- Tang, R. and Muller, H. G. (2008) Pairwise curve synchronization for functional data. *Biometrika*, **95**, 875–889.
- Telesca, D. and Inoue, L. Y. T. (2008) Bayesian hierarchical curve registration. *Journal of the American Statistical Association*, **103**, 328–339.
- Wang, X. and Berger, J. O. (2016) Estimating shape constrained functions using gaussian processes. *SIAM/ASA Journal on Uncertainty Quantification*, **4**, 1–25.

Wegman, E. J. (1970) Maximum likelihood estimation of a unimodal density, II. *Ann. Math. Stat.*, **41**, 2169–2174.
Zomorodian, A. and Carlsson, G. (2005) Computing persistent homology. *Discrete and Computational*

Geometry, **33**, 249–274.